

## The isothermal equation of state of CaPtO<sub>3</sub> post-perovskite to 40 GPa

Alex Lindsay-Scott<sup>a</sup>, Ian G. Wood<sup>a,\*</sup>, David P. Dobson<sup>a</sup>, Lidunka Vočadlo<sup>a</sup>, John P. Brodholt<sup>a</sup>, Wilson Crichton<sup>b,a</sup>, Michael Hanfland<sup>b</sup>, Takashi Taniguchi<sup>c</sup>

<sup>a</sup> Department of Earth Sciences, University College London, Gower Street, London, UK

<sup>b</sup> European Synchrotron Research Facility, Grenoble, France

<sup>c</sup> National Institute for Materials Science, Tsukuba, Ibaraki, Japan

### ARTICLE INFO

#### Article history:

Received 23 March 2010

Received in revised form 2 July 2010

Accepted 2 July 2010

Edited by: G. Helffrich.

#### Keywords:

CaPtO<sub>3</sub>

CaPt<sub>3</sub>O<sub>4</sub>

Post-perovskite

Equation of state

X-ray powder diffraction

### ABSTRACT

ABX<sub>3</sub> post-perovskite phases that are stable (or strongly metastable) at room-pressure are of importance as analogues of post-perovskite MgSiO<sub>3</sub>, a deep-Earth phase stable only at very high pressure. Commonly, CaIrO<sub>3</sub> has been used for this purpose, but it has been suggested that CaPtO<sub>3</sub> might provide a better analogue. We have measured the isothermal compressibility, at ambient temperature, of orthorhombic post-perovskite-structured CaPtO<sub>3</sub> to 40 GPa by X-ray powder diffraction using synchrotron radiation. A third-order Birch–Murnaghan equation of state fitted to the experimental data yields  $V_0 = 228.10(2) \text{ \AA}^3$ ,  $K_0 = 168.2(8) \text{ GPa}$  and  $K'_0 = 4.51(6)$ . Similar fits to the cube of each axis of the unit cell shows that the *b*-axis is the most compressible ( $b_0 = 9.9191(5) \text{ \AA}$ ,  $K_0 = 123.3(5) \text{ GPa}$ ,  $K'_0 = 2.37(3)$ ); the *a*-axis ( $a_0 = 3.12777(8) \text{ \AA}$ ,  $K_0 = 195.7(8) \text{ GPa}$ ,  $K'_0 = 6.63(8)$ ) and *c*-axis ( $c_0 = 7.3551(4) \text{ \AA}$ ,  $K_0 = 192(2) \text{ GPa}$ ,  $K'_0 = 12.2(3)$ ) are both much stiffer and have almost identical incompressibilities when the material is close to ambient pressure, but the *c*-axis shows greater stiffening on compression. Comparison of these axial incompressibilities with those of CaIrO<sub>3</sub> shows that CaPtO<sub>3</sub> is slightly less anisotropic under compression (possibly because of the absence of Jahn–Teller distortion), suggesting that CaPtO<sub>3</sub> may be a somewhat better analogue of MgSiO<sub>3</sub>.

Our sample also contained minor amounts of a cubic Ca<sub>3</sub>Pt<sub>3</sub>O<sub>4</sub> phase, for which the third-order Birch–Murnaghan equation-of-state parameters were found to be:  $V_0 = 186.00(3) \text{ \AA}^3$ ,  $K_0 = 213(1) \text{ GPa}$  and  $K'_0 = 4.9(1)$ .

© 2010 Elsevier B.V. All rights reserved.

### 1. Introduction

Perovskite-structured (PV) MgSiO<sub>3</sub> transforms to an orthorhombic CaIrO<sub>3</sub>-structured post-perovskite (PPV) phase at around 120 GPa (Murakami et al., 2004; Oganov and Ono, 2004). The atomic arrangement in the PPV phase of MgSiO<sub>3</sub> differs greatly from that found in PV-MgSiO<sub>3</sub> and thus one might expect that the physical properties of the two phases will also differ appreciably. The perovskite phase of MgSiO<sub>3</sub> contains the 3-dimensional network of corner-linked octahedra found in all perovskites. In contrast, the structure of ABO<sub>3</sub> post-perovskites is commonly described in terms of sheets of corner- and edge-sharing octahedra, lying parallel to (0 1 0), separated by planar A-cation interlayers. These features are illustrated in Fig. 1, which shows the crystal structure of the post-perovskite phase of CaIrO<sub>3</sub>, viewed down the *a*-axis; however, as discussed further below (Section 4) this view of the post-perovskite structure in terms of layers is almost certainly too simplistic.

The pressure at which the phase transition in MgSiO<sub>3</sub> occurs implies that post-perovskite MgSiO<sub>3</sub> might be the majority phase in the D'' region that extends into the mantle from the core–mantle boundary. If this is the case, then the physical and chemical properties of post-perovskite are likely to dominate the dynamics of much of the core–mantle boundary region.

Measurements of the physical and chemical properties of post-perovskite MgSiO<sub>3</sub> are difficult to perform because it is stable only at megabar pressures and so it has been more practical to obtain some of the experimental results required for comparison with computer simulations of PPV-structured MgSiO<sub>3</sub> from isostructural analogues whose compressive and thermal distortion at lower temperature and pressure are similar to those of MgSiO<sub>3</sub>. Analogues studied to date include CaIrO<sub>3</sub> (Boffa Ballaran et al., 2007; Lindsay-Scott et al., 2007; Martin et al., 2007a,b; Martin, 2008; Sugahara et al., 2008; Hirai et al., 2009) and CaPtO<sub>3</sub> (Inaguma et al., 2008; Ohgushi et al., 2008). CaIrO<sub>3</sub> may be synthesised at atmospheric pressure (see e.g. Lindsay-Scott et al., 2007). To date, synthesis of CaPtO<sub>3</sub> has been reported only at high pressures, in the range 4 GPa (Ohgushi et al., 2008) to 7 GPa (Inaguma et al., 2008). However, after synthesis, CaPtO<sub>3</sub> is readily recoverable to atmospheric pressure, where it remains stable, or at least very strongly metastable;

\* Corresponding author. Tel.: +44 020 7679 2405.

E-mail address: [ian.wood@ucl.ac.uk](mailto:ian.wood@ucl.ac.uk) (I.G. Wood).

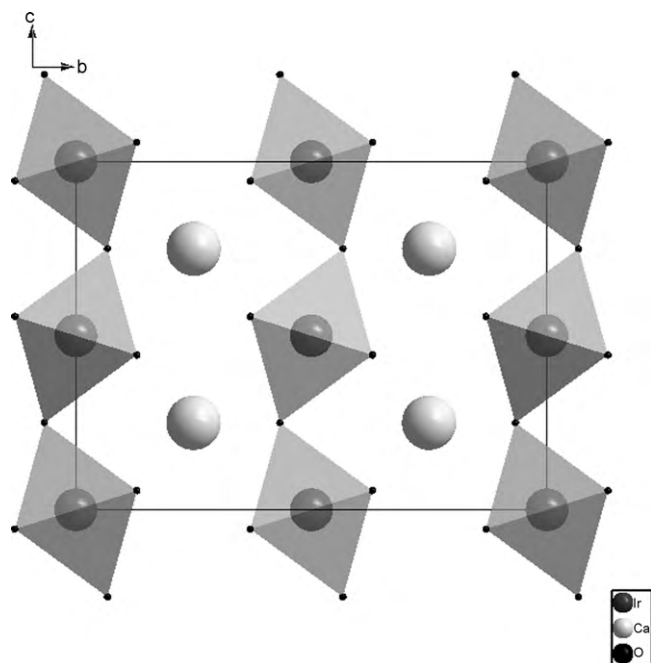


**Fig. 1.** The  $\text{CaIrO}_3$  post-perovskite type structure viewed along the  $a$ -axis. This structure is commonly described in the following way. Rods of edge-shared octahedra running parallel to the  $a$ -axis are linked into corrugated sheets by corner-sharing parallel to the  $c$ -axis, so as to produce sheets of  $\text{PtO}_6$  octahedra lying parallel to  $(010)$ ; these sheets are then separated along the  $b$ -axis by planar interlayers of Ca ions. However, this view of the structure in terms of layers is almost certainly too simplistic (see Section 4 for further discussion).

for example, high-temperature X-ray powder diffraction measurements in our laboratory (unpublished) have shown that it persists, in air, for periods of longer than 1 h at temperatures as high as  $800^\circ\text{C}$ .  $\text{CaPtO}_3$  is of interest because, unlike  $\text{CaIrO}_3$ , it does not exhibit structural distortion due to the Jahn-Teller effect and thus it has been suggested that it might provide a better analogue of  $\text{MgSiO}_3$  (Ohgushi et al., 2008). Boffa Ballaran et al. (2007) and Martin et al. (2007a) have measured the bulk and axial incompressibilities of  $\text{CaIrO}_3$ , but  $\text{CaPtO}_3$  has been studied only at ambient pressure and temperature (Ohgushi et al., 2008; Inaguma et al., 2008). In this paper we report measurements of  $\text{CaPtO}_3$  to 40 GPa in order to assess the similarity of its behaviour under compression to that of  $\text{CaIrO}_3$  and  $\text{MgSiO}_3$ .

## 2. Experimental method

The sample was synthesized under high pressure and high temperature using a belt-type high-pressure apparatus at the National Institute for Materials Science, Tsukuba, Ibaraki, Japan. The starting material was a stoichiometric powder mixture of  $\text{PtO}_2$  and  $\text{CaO}$ , ground together in a mortar and sealed in a Pt capsule. This was then compressed to 4 GPa, heated to  $800^\circ\text{C}$  for 24 h and then quenched to room temperature prior to slow decompression. The recovered dark-yellow powder was characterized by X-ray powder diffraction. The sample for this X-ray analysis was prepared as a thin smear on an “off-axis” silicon plate (i.e. one cut so as to produce no Bragg reflections) and the powder pattern was recorded using a PANalytical X’Pert Pro diffractometer with  $\text{Co K}\alpha_1$  radiation (40 kV, 30 mA), scanning over the range  $10^\circ < 2\theta < 90^\circ$ . The sample was found to contain orthorhombic  $\text{CaPtO}_3$  ( $Cmcm$ ;  $a = 3.12612(2)\text{ \AA}$ ,  $b = 9.91709(6)\text{ \AA}$ ,  $c = 7.34952(5)\text{ \AA}$ ,  $V = 227.850(2)\text{ \AA}^3$ ), with minor amounts of cubic  $\text{Ca}_x\text{Pt}_3\text{O}_4$  ( $Pm\bar{3}n$ ;  $a = 5.7064(1)\text{ \AA}$ ,  $V = 185.82(1)\text{ \AA}^3$ ; Bergner and Kohlhaas, 1973) and traces of cubic Pt ( $Fm\bar{3}m$ ;  $a = 3.9262(2)\text{ \AA}$ ,  $V = 60.52(1)\text{ \AA}^3$ ; Holmes

et al., 1989). The lattice parameters for the  $\text{CaPtO}_3$  (estimated from a Le Bail refinement of the data, see below) were found to be in reasonable agreement with those previously reported at ambient pressure and temperature (see Table 1a). Our values are much closer to those of Ohgushi et al. (2008) than those of Inaguma et al. (2008); however, when comparing these results it should be remembered that, due to the lack of an internal standard and limited  $2\theta$  range, they are likely to be less accurate on an absolute scale than their precision might otherwise suggest (although it should, in principle, have been possible to use the platinum present in our sample as an internal standard, in practice there was insufficient platinum present to allow this to be done reliably in any of our experiments).

A selected portion of the sample was loaded, with a helium pressure medium, into a  $150\text{-}\mu\text{m}$ -diameter hole in a  $400\text{-}\mu\text{m}$ -thick steel gasket mounted between two opposed  $300\text{-}\mu\text{m}$  diamond culets of a Böhler-Almax-type membrane-driven diamond-anvil cell. Pressures were determined from the shift of the wavelength of the ruby- $R_1$  fluorescence line, using the recent pressure-scale calibration of Jacobsen et al. (2008) for helium pressure media. Ruby fluorescence measurements were made before and after collection of each diffraction pattern, with the ruby- $R_1$  wavelength at the data point taken as the mean value of these two readings. The uncertainty in the pressure, due to relaxation of the cell during the collection of each diffraction pattern, was estimated from the difference in the two ruby measurements, in combination with the quoted uncertainty in the  $B$ -parameter in the equation relating the pressure to the ruby- $R_1$  wavelength-shift (Jacobsen et al., 2008); see Table 1b for further details.

Diffraction patterns were collected on the ID09 beamline at the ESRF, using a monochromatic wavelength of  $0.41456\text{ \AA}$  on a mar555 image plate detector. The detector was positioned at  $358.71\text{ mm}$  from the sample, so as to cover a range  $0^\circ < 2\theta < 37.9^\circ$ ; the exposure time was  $\sim 1\text{ s}$ . Data were collected with increasing pressure from  $2.90(2)\text{ GPa}$  to  $42.50(4)\text{ GPa}$ , with a final pattern recorded at  $1.21(1)\text{ GPa}$  after decompression. The  $2\theta$  vs intensity patterns used in the powder refinement were obtained by integrating around the Debye–Scherrer rings, after correction for detector distortion and tilt, using the Fit2D package (Hammersley et al., 1995). The diffraction patterns were then fitted, over the range  $3.16^\circ < 2\theta < 33.2^\circ$ , to obtain unit-cell parameters using the Le Bail method (Le Bail et al., 1988) implemented in the GSAS suite of programs (Larson and Von Dreele, 1994) with the EXPGUI graphical interface (Toby, 2001). The lineshape used in the GSAS refinements was “profile function number 2”, which is based on a pseudo-Voigt function (Larson and Von Dreele, 1994). At pressures above  $12.6\text{ GPa}$  diffraction peaks characteristic of hexagonal ( $P6_3/mmc$ ) He crystals were observed (Mao et al., 1988) and so this phase was also included in the refinements. Examples of the fitted diffraction patterns at  $2.90(2)\text{ GPa}$  and  $42.50(4)\text{ GPa}$  are shown in Fig. 2. It can be seen that the Bragg reflections in Fig. 2B are broader, due to the development of non-hydrostatic stresses; after decompressing the sample the widths of the reflections returned to their original low-pressure values. The onset of this line broadening is clearly indicated in the refined values of the GSAS profile parameters; these are effectively invariant until  $\sim 16\text{ GPa}$ , but at higher pressures the values of some of the profile coefficients alter systematically. In particular, the coefficient  $U$  (which affects the Gaussian variance of the Bragg peaks via a term in  $U \tan^2(\theta)$ ; Caglioti et al., 1958) increases, with the increase becoming marked above  $\sim 22\text{ GPa}$ , an effect that can be attributed to non-uniform strain in the crystallites (Larson and Von Dreele, 1994). Possible sources of non-hydrostatic stresses in the experiment are solidification of the He pressure medium and grain–grain interactions in the  $\text{CaPtO}_3$  sample. This line broadening does not appear to lead to any systematic errors in the refined values of the cell parameters (see Figs. 3 and 4), but it does increase their esti-

**Table 1a**

Unit-cell parameters and unit-cell volume for CaPtO<sub>3</sub> at ambient pressure and temperature; the numbers in parentheses are estimated standard uncertainties and refer to the least-significant digits. The value quoted for the present work is that measured in our laboratory at UCL with Co K $\alpha_1$  radiation (see Section 2).

	<i>a</i> (Å)	<i>b</i> (Å)	<i>c</i> (Å)	Volume (Å <sup>3</sup> )
Present work	3.12612(2)	9.91709(6)	7.34952(5)	227.850(2)
Ohgushi et al. (2008)	3.12607(1)	9.91983(4)	7.35059(3)	227.942(2)
Inaguma et al. (2008)	3.1232(4)	9.912(1)	7.3459(9)	227.41(5)

mated uncertainties, which are greater by about a factor of seven at ~40 GPa than at pressures below ~7 GPa (Table 1b).

### 3. Results

The observed unit-cell parameters and unit-cell volume of CaPtO<sub>3</sub> between 1.21(1) GPa and 42.50(4) GPa are listed in Table 1b. Fig. 3 shows the change in volume with pressure and Fig. 4 shows the relative compression of the three unit-cell edges, plotted as the cube of the axial compression ratios. It can be seen from Fig. 4 that the compression is strongly anisotropic, being greatest for the *b*-axis (i.e. for the direction perpendicular to the sheets of PtO<sub>6</sub> octahedra and Ca-ion interlayers) and smallest for the *c*-axis (i.e. along the chains of apex-linked PtO<sub>6</sub> octahedra). The data, including the decompression data point, both for the unit-cell volume and for the cubes of the unit-cell axes, were fitted to third-order Birch–Murnaghan equations of state (Birch, 1978) by non-linear least-squares using the EOS-fit program (Angel, 2000, 2001); the weighting scheme in the refinement used weights calculated from the errors in both the pressure and in the unit-cell volume and lattice parameters. The resulting values of the three equation-of-state parameters for each of the four fits are listed in Table 2. The values of *V*<sub>0</sub>, *a*<sub>0</sub>, *b*<sub>0</sub>, and *c*<sub>0</sub> thereby obtained are consistent both with

the lattice parameters of CaPtO<sub>3</sub> from previous powder diffraction studies at ambient pressure (Ohgushi et al., 2008; Inaguma et al., 2008) and with those that we obtained in the present study during the sample characterisation (there is, however, clearly a slight systematic offset between our two diffraction experiments as all of the values from the high-pressure study are slightly higher, by 0.1% for the unit-cell volume and 0.02–0.07% for the unit-cell edges). The good internal consistency of the high-pressure data sets can be demonstrated in two ways. Firstly, the values from the non-linear least-squares fit of the volumetric incompressibility (*K*<sub>0</sub>) and of its first derivative with respect to pressure (*K*'<sub>0</sub>) of 168.2(8) GPa and 4.51(6), respectively, are in good agreement with the corresponding values of 168.4(4) GPa and 4.47(4) obtained by weighted linear regression from the *f*–*F* plot (see e.g. Angel, 2000) that is shown as an inset in Fig. 3. In this method of analysis, the incompressibility at zero pressure is obtained from a weighted linear fit of the normalised stress  $F_E = P/(3f_E(1 + 2f_E)^{5/2})$  against finite strain,  $f_E = 0.5[(V_0/V)^{2/3} - 1]$ . Secondly, the value of *V*<sub>0</sub> obtained from the product of *a*<sub>0</sub>, *b*<sub>0</sub>, and *c*<sub>0</sub> is 228.19(2) Å<sup>3</sup>, which differs by 0.09(3) Å<sup>3</sup> from that obtained when the volume is fitted directly.

In addition to the CaPtO<sub>3</sub>, there was sufficient of the cubic Ca<sub>x</sub>Pt<sub>3</sub>O<sub>4</sub> phase present in the sample to allow reliable determination of its cell parameter. By fitting the unit-cell volume to a third-order Birch–Murnaghan equation of state, as described above, we obtained the following values: *V*<sub>0</sub> = 186.00(3) Å<sup>3</sup>; *K*<sub>0</sub> = 213(1) GPa; *K*'<sub>0</sub> = 4.9(1). When considering these results, which are reported here for completeness, it should, however, be remembered that this material has been reported to be of variable stoichiometry, with 0 ≤ *x* ≤ 1 (Bergner and Kohlhaas, 1973).

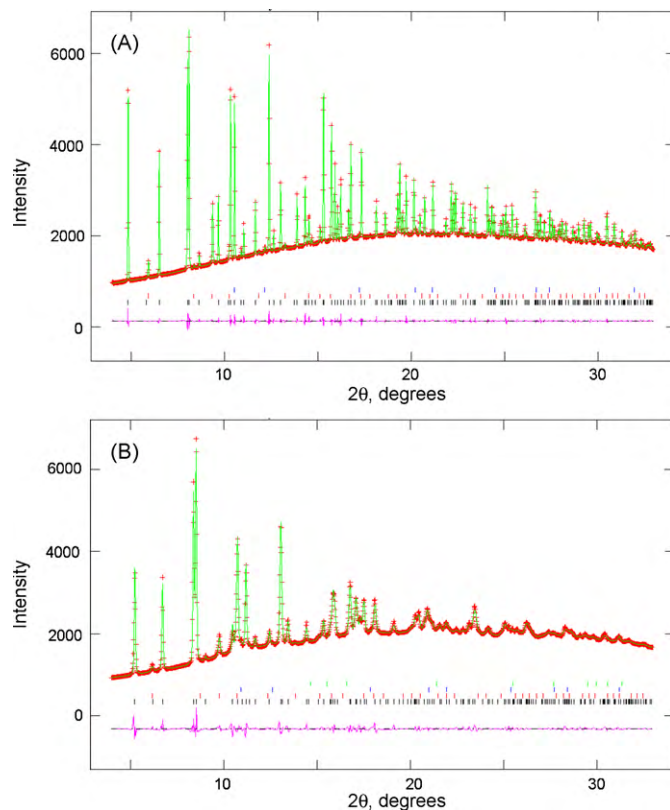


**Fig. 2.** Observed (points), calculated (line) and difference (lower trace) X-ray powder diffraction patterns ( $\lambda = 0.41456 \text{ \AA}$ ) for CaPtO<sub>3</sub> at: (A) 2.90(2) GPa and (B) 42.50(4) GPa. The tick marks show the positions of the Bragg reflections of (from the bottom upwards): CaPtO<sub>3</sub>, CaPt<sub>3</sub>O<sub>4</sub>, Pt and (B only) He.

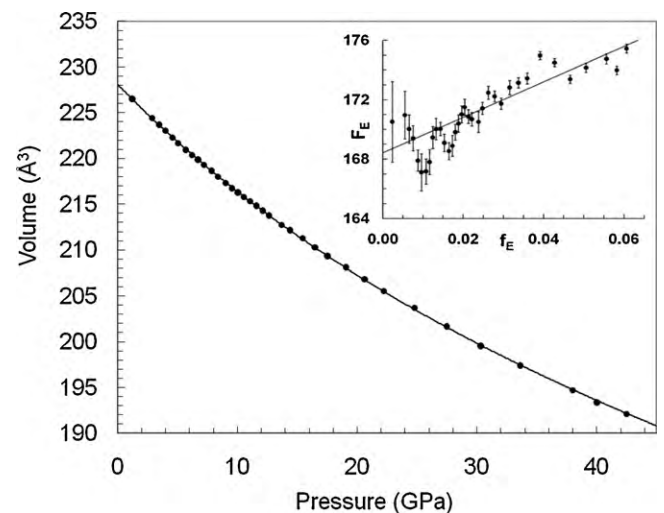


**Fig. 3.** Unit-cell volume of CaPtO<sub>3</sub> between 1.21(1) GPa and 42.50(4) GPa. Experimental values are shown as points (error bars are smaller than the symbols used). The full line shows the fit of the data to a third-order Birch–Murnaghan equation of state (see text for details). The inset shows the *f*–*F* plot for these data, calculated using the value of *V*<sub>0</sub>, 228.10(2) Å<sup>3</sup>, from this fit (Table 2). The solid line shown in the inset is a weighted linear fit with  $F_E = 120(11)f_E + 168.4(4) \text{ GPa}$ . The value of the incompressibility, *K*<sub>0</sub>, is equal to the intercept on the *y*-axis of the *f*–*F* plot; the value of its first derivative with respect to pressure, *K*'<sub>0</sub>, is obtained via the relationship that the slope of the *f*–*F* plot is equal to  $3K_0(K'_0 - 4)/2$  (Angel, 2000; see Section 3 for further details).

**Table 1b**

Unit-cell parameters and unit-cell volume for CaPtO<sub>3</sub> as a function of pressure, as measured in the diamond-anvil cell at the ESRF. The data were recorded in the order shown. The numbers in parentheses are estimated standard uncertainties and refer to the least-significant digits.

P (GPa)	a (Å)	b (Å)	c (Å)	Volume (Å <sup>3</sup> )
2.90(2)	3.11291(2)	9.84590(9)	7.32129(6)	224.393(4)
3.45(1)	3.11050(2)	9.83073(9)	7.31545(6)	223.695(4)
3.98(1)	3.10794(2)	9.81702(9)	7.31008(6)	223.036(4)
4.59(1)	3.10502(2)	9.80079(7)	7.30368(5)	222.263(2)
5.05(3)	3.10275(2)	9.78895(9)	7.29884(6)	221.685(4)
5.69(2)	3.09984(2)	9.77312(9)	7.29270(6)	220.933(4)
6.20(2)	3.09763(2)	9.76146(9)	7.28801(6)	220.370(4)
6.71(2)	3.09572(2)	9.75077(9)	7.28391(6)	219.869(4)
7.22(2)	3.09357(3)	9.73904(10)	7.27951(7)	219.320(4)
7.84(1)	3.09084(3)	9.72520(10)	7.27384(6)	218.645(4)
8.37(2)	3.08839(3)	9.71204(11)	7.26870(7)	218.021(5)
9.02(2)	3.08566(3)	9.69559(11)	7.26296(7)	217.288(5)
9.55(3)	3.08358(3)	9.68384(10)	7.25855(7)	216.747(5)
10.04(2)	3.08195(3)	9.67358(10)	7.25490(7)	216.290(4)
10.55(3)	3.08001(3)	9.66289(10)	7.25109(7)	215.805(4)
11.08(3)	3.07811(3)	9.65200(11)	7.24707(7)	215.310(5)
11.59(3)	3.07627(3)	9.64136(11)	7.24333(7)	214.833(5)
12.10(2)	3.07409(3)	9.62936(12)	7.23903(8)	214.287(5)
12.62(3)	3.07204(3)	9.61759(12)	7.23493(8)	213.761(5)
13.70(5)	3.06793(4)	9.59463(13)	7.22645(9)	212.715(6)
14.38(2)	3.06576(4)	9.58160(13)	7.22187(9)	212.142(6)
15.43(3)	3.06221(4)	9.56182(16)	7.21496(11)	211.256(7)
16.46(2)	3.05840(4)	9.54021(15)	7.20764(11)	210.303(7)
17.52(3)	3.05471(5)	9.51746(18)	7.20009(12)	209.329(8)
19.06(4)	3.04976(6)	9.48918(22)	7.19095(15)	208.104(10)
20.62(3)	3.04465(6)	9.45945(23)	7.18141(15)	206.830(10)
22.22(4)	3.03963(7)	9.42972(28)	7.17183(18)	205.565(12)
24.79(2)	3.03231(9)	9.38640(37)	7.15781(25)	203.729(17)
27.46(2)	3.02459(11)	9.33593(40)	7.14297(30)	201.699(19)
30.30(2)	3.01617(13)	9.28288(52)	7.12716(33)	199.551(23)
33.61(4)	3.00811(14)	9.22671(55)	7.11284(37)	197.416(26)
37.98(5)	2.99721(16)	9.15550(64)	7.09562(42)	194.710(29)
40.02(3)	2.99209(16)	9.11863(64)	7.08734(43)	193.369(29)
42.50(4)	2.98668(15)	9.08541(61)	7.07981(42)	192.112(28)
1.21(1)	3.12155(4)	9.88679(14)	7.33933(9)	226.507(6)

In (b) above, the pressure values were obtained from the relative shift of the wavelength of the ruby-R<sub>1</sub> fluorescence line ( $\Delta\lambda/\lambda_0$ ), using the equation  $P$  (GPa) =  $(A/B)\{[1 + (\Delta\lambda/\lambda_0)]^B - 1\}$ , where  $A = 1904$  GPa and  $B = 10.32(7)$  (Jacobsen et al., 2008). Ruby measurements were made before ( $\lambda_a$ ) and after ( $\lambda_b$ ) each diffraction pattern was recorded and the value of  $\Delta\lambda$  was then calculated using their mean. The uncertainties in the pressure values were derived assuming that the uncertainty in the fluorescence wavelength was  $(\lambda_a - \lambda_b)/4$  (i.e. that the observations corresponded to a mean value  $\pm$  two standard uncertainties); the uncertainty in the parameter  $B$  given by Jacobsen et al. (2008) was also included in the calculation. Note that in both Table 1a and Table 1b the lattice parameter values listed are probably less accurate than might be expected from the stated uncertainties, which are as reported by the Le Bail fits using GSAS; for further discussion of the importance of systematic errors in profile refinement of X-ray powder data see e.g. Thompson and Wood (1983).

**Table 2**

Equation-of-state parameters obtained by fitting the data shown in Table 1b to third-order Birch–Murnaghan equations of state. For the unit-cell edges, the values of  $K_0$  and  $K'_0$  are those obtained by fitting to the cubes of the lengths of the unit-cell edges (for details see text).

	$V_0$ (Å <sup>3</sup> )	$K_0$ (GPa)	$K'_0$
Volume	228.10(2)	168.2(8)	4.51(6)
a-axis	3.12777(8)	195.7(8)	6.63(8)
b-axis	9.9191(5)	123.3(5)	2.37(3)
c-axis	7.3551(4)	192(2)	12.2(3)

For comparison with the results of Martin et al. (2007a) the unit-cell volumes were also fitted to a second-order Birch–Murnaghan equation of state. The resulting values of  $V_0$  and  $K_0$  were 227.95(2) Å<sup>3</sup> and 174.0(5) GPa respectively (with  $K'_0$  fixed at 4).

(Note that if the commonly used ruby fluorescence pressure scale of Mao et al. (1986) is employed, instead of that of Jacobsen et al. (2008), the volumetric equation-of-state parameters then become  $V_0 = 228.09(2)$  Å<sup>3</sup>,  $K_0 = 168.8(8)$  GPa and  $K'_0 = 4.16(6)$  respectively. The more recent ruby scale of Dewaele et al. (2004), gives values that are not significantly different from those shown in the table above, with  $V_0 = 228.10(2)$  Å<sup>3</sup>,  $K_0 = 168.5(8)$  GPa and  $K'_0 = 4.39(6)$ ).

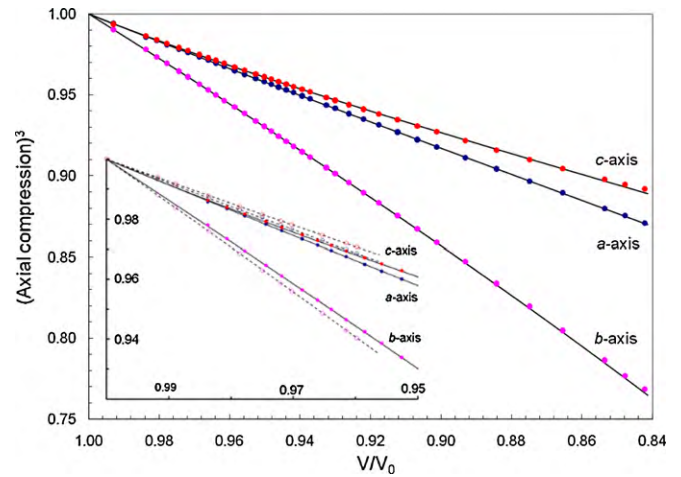


**Fig. 4.** Axial compressions,  $i/i_0$  (where  $i = a, b$  or  $c$  unit-cell parameter), of CaPtO<sub>3</sub>, plotted as the ratios  $(i/i_0)^3$ . The symbols denote the experimentally observed axial and volumetric values. The lines are derived from the axial equations of state, plotted against values of  $V/V_0$  calculated from the volumetric equation of state (Table 2). The inset to the figure shows a comparison of the values for CaPtO<sub>3</sub> (solid symbols and lines) with those for CaIrO<sub>3</sub> (open symbols and broken lines), as determined by Boffa Ballaran et al. (2007).

#### 4. Discussion

The only equation-of-state parameters for CaPtO<sub>3</sub> with which to compare the results of the present study are those of Matar et al. (2008) who carried out an investigation of both PPV- and PV-structured CaPtO<sub>3</sub> by athermal *ab initio* computer simulations within the local density approximation (LDA). The agreement of our experimental values  $\{V_0 = 228.10(2)$  Å<sup>3</sup>;  $K_0 = 168.2(8)$  GPa;  $K'_0 = 4.51(6)\}$  with those from this simulation is surprisingly poor, as Matar et al. (2008) obtained  $V_0 = 212.14(5)$  Å<sup>3</sup> and  $K_0 = 222(1)$  GPa, with  $K'_0 = 4.59(8)$ . Although LDA calculations commonly overestimate the binding of the atoms and hence lead to calculated unit-cell parameters that are smaller than the experimental values, the discrepancy of 7% in  $V_0$  is very large; similarly the value of  $K_0$  from the computer simulations is over 30% greater than our experimental value (note, however, that if the equation-of-state parameters of Matar et al. are used to calculate  $K$  at the experimental value of  $V_0$  a value of 157 GPa is obtained, in much closer agreement with our experimental result). The reasons for this poor agreement are not clear, especially as Matar et al. (2008) also state that test calculations carried out using the generalised gradient approximation (GGA), which commonly leads to an overestimate of the unit-cell volume, did not produce any significant improvement in the agreement between their calculated volume and the available experimental results. It is, perhaps, possible that the discrepancy is simply due to the lack of state points in the calculations, which appear to have been carried out at only six volumes, of which only two were for the material under compression. Unfortunately, no lattice parameters are given by Matar et al. (2008), only unit-cell volumes, and so it is impossible to determine whether their calculations produced a general underestimate of all three cell parameters or whether they failed to reproduce correctly the axial ratios of the crystal.

It is also of interest to compare the present results with the experimental values of the equation-of-state parameters for the other low-pressure post-perovskite analogue phase, CaIrO<sub>3</sub>. We have found that PPV-CaPtO<sub>3</sub> has a slightly larger unit-cell volume and lower value of  $K_0$  than PPV-CaIrO<sub>3</sub>. Boffa Ballaran et al. (2007) fitted a third-order Birch–Murnaghan equation to single-crystal X-ray data from PPV-CaIrO<sub>3</sub>, obtaining  $V_0 = 226.38(1)$  Å<sup>3</sup> and  $K_0 = 181(3)$  GPa, with  $K'_0 = 2.3(8)$ . Although the uncertainty is

large, the value of  $K'_0$  for  $\text{CaIrO}_3$  is significantly lower than our corresponding value for  $\text{CaPtO}_3$ . Boffa Ballaran et al. (2007) used methanol–ethanol as their pressure medium, and the ruby scale of Mao et al. (1986); however, the difference in  $K'_0$  cannot be attributed simply to differences in the pressure scale, since if we apply the ruby scale of Mao et al. (1986) to our data (see Table 2) we still obtain a value of  $K'_0$  that is significantly higher than that of  $\text{CaIrO}_3$ . Other previous measurements of the compression of PPV- $\text{CaIrO}_3$  are those obtained using X-ray powder diffraction by Martin et al. (2007a) who fitted a second-order Birch–Murnaghan equation, giving  $V_0 = 226.632(45) \text{ \AA}^3$  and  $K_0 = 180.2(3) \text{ GPa}$ ; our corresponding values for PPV- $\text{CaPtO}_3$  ( $V_0 = 227.95(2) \text{ \AA}^3$ ,  $K_0 = 174.0(5) \text{ GPa}$ , with  $K'_0$  fixed at 4; see Table 2) show an increase in  $V_0$  and decrease in  $K_0$  similar to that discussed above, although, as  $K'_0$  is fixed at 4 in both cases, the differences in the two fitted parameters are now not as large.

A further contrast in the behaviour of  $\text{CaPtO}_3$  and  $\text{CaIrO}_3$  lies in the relative unit-cell volumes and incompressibilities of the PPV- and PV-structured forms of the two materials. For  $\text{CaIrO}_3$ , Boffa Ballaran et al. (2007) found experimentally that, at zero pressure, the ratio of the volumes of the PPV- and PV-structured phases was 0.98656(6) and that the PV-structured phase, with  $K_0 = 198(3) \text{ GPa}$  and  $K'_0 = 1.2(8)$ , was stiffer (at ambient pressure) than the PPV-structured phase. For  $\text{CaPtO}_3$ , the computer simulations of Matar et al. (2008), showed that, at zero pressure, the PPV- and PV-structured phases have a similar volume ratio to that of  $\text{CaIrO}_3$ , 0.9878(13), but in this case the PV-structured material is softer, with  $K_0 = 205(1) \text{ GPa}$  and  $K'_0 = 4.42(5)$ . However, this apparent difference in behaviour should probably be treated with caution. No experimental data for a PV-structured phase of  $\text{CaPtO}_3$  have, as yet, been presented and in view of the discrepancy of the *ab initio* results with our experimental values for PPV- $\text{CaPtO}_3$  it is probably unwise to rely upon them too closely.

The axial incompressibilities of  $\text{CaPtO}_3$  are similar in form to those of  $\text{CaIrO}_3$ . The *a*-axis and *c*-axis of  $\text{CaPtO}_3$  have the same incompressibility (within experimental uncertainty) at ambient pressure, but the *c*-axis stiffens faster than the *a*-axis, having a value of  $K'_0$  that is greater by almost a factor of two; in contrast, the *b*-axis is much softer. If the crystal structure of PPV- $\text{CaPtO}_3$  is viewed in a naive way in terms of layers of  $\text{PtO}_6$  octahedra separated by planar Ca-cation interlayers, a ready explanation is afforded for the relative softness of the *b*-axis by the reduction of the interlayer spacing. However, on this basis it is difficult to explain why the *c*-axis is the least compressible direction in the crystal, since this axis should then be readily shortened by buckling of the planes of corner-linked octahedra, whereas to reduce the length of the *a*-axis must involve distortion of the  $\text{PtO}_6$  octahedra through shortening of the O–O distances aligned parallel to the *a*-axis. Clearly, therefore, this view of the response to compression of post-perovskite structures in terms of layers and interlayers is too simplistic, but to properly address this question requires an accurate set of atomic coordinates as a function of pressure, which is not yet available. In connection with this discussion, it is interesting to note also that, at least in the case of  $\text{CaIrO}_3$ , the response of the PPV-structure to heat is not simply the inverse of the response to pressure; thus, although the *b*-axis of  $\text{CaIrO}_3$  expands most on heating, the expansion of the *c*-axis is far larger than that of the *a*-axis (Lindsay-Scott et al., 2007; Martin et al., 2007a).

In Table 3, the ratios of the axial incompressibilities with respect to that of the *c*-axis, for both  $\text{CaPtO}_3$  and  $\text{CaIrO}_3$ , are compared to those for  $\text{MgSiO}_3$  and  $\text{Mg}_{0.6}\text{Fe}_{0.4}\text{SiO}_3$ . The low incompressibility ratio of the *b*-axis relative to that of the *c*-axis, found in both  $\text{CaPtO}_3$  and  $\text{CaIrO}_3$ , is similar in magnitude to that reported for  $\text{MgSiO}_3$  at pressures and temperatures comparable to those that would obtain in the *D''* region of the Earth's mantle (Guignot et al., 2007). However, much worse agreement is found with the axial

**Table 3**

Axial incompressibility ratios of some post-perovskite phases.

	$K_a/K_c$	$K_b/K_c$
$\text{CaPtO}_3$ (ambient <i>P</i> , <i>T</i> ) <sup>a</sup>	1.02(1)	0.64(1)
$\text{CaIrO}_3$ (ambient <i>P</i> , <i>T</i> ) <sup>b</sup>	0.94(3)	0.51(1)
$\text{MgSiO}_3$ (135 GPa, 4000 K) <sup>c</sup>	0.84(6)	0.58(4)
$\text{Mg}_{0.6}\text{Fe}_{0.4}\text{SiO}_3$ (140 GPa, ambient <i>T</i> ) <sup>d</sup>	1.05 <sup>e</sup>	0.91 <sup>e</sup>

<sup>a</sup> This work.<sup>b</sup> Boffa Ballaran et al. (2007).<sup>c</sup> Guignot et al. (2007).<sup>d</sup> Mao et al. (2010).<sup>e</sup> Uncertainties not given.

incompressibility ratios for  $\text{Mg}_{0.6}\text{Fe}_{0.4}\text{SiO}_3$  at 140 GPa and ambient temperature (Mao et al., 2010); in this case, although the value for  $K_a/K_c$  agrees well with that from  $\text{CaPtO}_3$ , neither  $\text{CaPtO}_3$  nor  $\text{CaIrO}_3$  give a similar value for  $K_b/K_c$  (though the agreement for  $\text{CaPtO}_3$  is somewhat better than for  $\text{CaIrO}_3$ ). A more detailed comparison of the axial compressions of  $\text{CaPtO}_3$  with previously published results for  $\text{CaIrO}_3$  (Boffa Ballaran et al., 2007) is shown as an inset to Fig. 4. Clearly, at all pressures,  $\text{CaPtO}_3$  is slightly less elastically anisotropic than  $\text{CaIrO}_3$ . This difference in anisotropy may be due to distortion of the  $\text{IrO}_6$  octahedra in  $\text{CaIrO}_3$ , caused by the Jahn-Teller effect (Ohgushi et al., 2008); the absence of this effect in  $\text{CaPtO}_3$  may indicate that it is, therefore, a somewhat better analogue for  $\text{MgSiO}_3$  post-perovskite at low pressure and temperature.

## Acknowledgments

AL-S is funded by a postgraduate studentship from the Natural Environment Research Council. Shaun Evans is thanked for experimental assistance at ID09. We are also grateful for the helpful comments of an anonymous referee with regard to the choice of pressure scale.

## References

- Angel, R.J., 2000. Equations of state. In: Hazen, R.M., Downs, R.T. (Eds.), Reviews in Mineralogy and Geochemistry, vol. 41. Mineral. Soc. Am., Washington.
- Angel, R.J., 2001. EOS-FIT V5. 2. Computer program. Crystallography Laboratory, Department of Geological Sciences, Virginia Tech, Blacksburg, VA, USA.
- Bergner, D., Kohlhaas, R., 1973. Neue Verbindungen vom  $\text{Na}_x\text{Pt}_3\text{O}_4$ -Strukturtyp. Z. Anorg. Allg. Chem. 401, 15–20.
- Birch, F., 1978. Finite strain isotherm and velocities for single crystal NaCl at high pressures and 300 degrees K. J. Geophys. Res. 83, 1257–1268.
- Boffa Ballaran, T., Tronnes, R.G., Frost, D.J., 2007. Equations of state of  $\text{CaIrO}_3$  perovskite and post-perovskite phases. Am. Mineral. 92, 1760–1763.
- Caglioti, G., Paoletti, A., Ricci, F.P., 1958. Choice of collimators for a crystal spectrometer for neutron diffraction. Nucl. Instrum. Methods 3, 223–228.
- Dewaele, A., Loubeyre, P., Mezouar, M., 2004. Equations of state of six metals above 94 GPa. Phys. Rev. B 70, 094112.
- Guignot, N., Andrault, D., Morard, G., Bolfan-Casanova, N., Mezouar, M., 2007. Thermoelastic properties of post-perovskite phase  $\text{MgSiO}_3$  determined experimentally at core–mantle boundary *P–T* conditions. Earth Planet. Sci. Lett. 256, 162–168.
- Hammersley, A.P., Svensson, S.O., Thompson, A., Graafsma, H., Kvick, A., Moy, J.P., 1995. Calibration and correction of distortion in two dimensional detector systems. Rev. Sci. Instrum. 66, 2729–2733.
- Hirai, S., Welch, M.D., Aguado, F., Redfern, S.A.T., 2009. The crystal structure of  $\text{CaIrO}_3$  post-perovskite revisited. Zeit. Krist. 224, 345–350.
- Holmes, N.C., Moriarty, J.A., Gathers, G.R., Nellis, W.J., 1989. The equation of state of platinum to 660 GPa (6.6 Mbar). J. Appl. Phys. 66, 2962–2967.
- Inaguma, Y., Hasumi, K., Yoshida, M., Ohba, T., Katsumata, T., 2008. High-pressure synthesis, structure, and characterization of a post-perovskite  $\text{CaPtO}_3$  with  $\text{CaIrO}_3$ -type structure. Inorg. Chem. 47, 1868–1870.
- Jacobsen, S.D., Holl, C.M., Adams, K.A., Fischer, R.A., Martin, E.S., Bina, C.R., Lin, J.-F., Prakapenka, V.B., Kubo, A., Dera, R., 2008. Compression of single-crystal magnesium oxide to 118 GPa and a ruby pressure gauge for helium pressure media. Am. Mineral. 93, 1823–1828.
- Larson, A.C., Von Dreele, R.B., 1994. General Structure Analysis System (GSAS), Los Alamos National Laboratory Report LAUR 86-748.
- Le Bail, A., Duroy, H., Fourquet, J.L., 1988. *Ab initio* structure determination of  $\text{LiSbWO}_6$  by X-ray powder diffraction. Mater. Res. Bull. 23, 447–452.
- Lindsay-Scott, A., Wood, I.G., Dobson, D., 2007. Thermal expansion of  $\text{CaIrO}_3$  determined by X-ray powder diffraction. Phys. Earth Planet. Inter. 162, 140–148.

- Mao, H.-K., Hemley, R.J., Wu, Y., Jephcoat, A.P., Finger, L.W., Zha, C.S., Bassett, W.A., 1988. High-pressure phase diagram and equation of state of solid helium from single-crystal X-ray diffraction to 23.3 GPa. *Phys. Rev. Lett.* 60, 2649–2652.
- Mao, H.-K., Xu, J., Bell, P.M., 1986. Calibration of the ruby pressure gauge to 800 kbar under quasi-hydrostatic conditions. *J. Geophys. Res.* 91, 4673–4676.
- Mao, W.L., Meng, Y., Mao, H.-K., 2010. Elastic anisotropy of ferromagnesian post-perovskite in Earth's D' layer. *Phys. Earth Planet. Inter.* 180, 203–208.
- Martin, C.D., 2008. The local post-perovskite structure and its temperature dependence: atom-pair distances in  $\text{CaIrO}_3$  revealed through analysis of the total X-ray scattering at high temperatures. *J. Appl. Cryst.* 41, 776–783.
- Martin, C.D., Chapman, K.W., Chupas, P.J., Prakapenka, V., Lee, P.L., Shastri, S.D., Parise, J.B., 2007a. Compression, thermal expansion, structure and instability of  $\text{CaIrO}_3$ , the structure model of  $\text{MgSiO}_3$  post-perovskite. *Am. Mineral.* 92, 1048–1053.
- Martin, C.D., Smith, R.I., Marshall, W.G., Parise, J.B., 2007b. High-pressure structure and bonding in  $\text{CaIrO}_3$ : the structure model of  $\text{MgSiO}_3$  post-perovskite investigated with time-of-flight neutron powder diffraction. *Am. Mineral.* 92, 1912–1918.
- Matar, S.F., Demazeau, G., Largeteau, A., 2008. Ab initio investigation of perovskite and post-perovskite  $\text{CaPtO}_3$ . *Chem. Phys.* 352, 92–96.
- Murakami, M., Hirose, K., Kawamura, K., Sata, N., Ohishi, Y., 2004. Post perovskite phase transition in  $\text{MgSiO}_3$ . *Science* 304, 855–858.
- Oganov, A.R., Ono, S., 2004. Theoretical and experimental evidence for a post-perovskite phase of  $\text{MgSiO}_3$  in Earth's D' layer. *Nature* 430, 445–448.
- Ohgushi, K., Matsushita, Y., Miyajima, N., Katsuya, Y., Tanaka, M., Izumi, F., Gotou, H., Ueda, Y., Yagi, T., 2008.  $\text{CaPtO}_3$  as a novel post-perovskite oxide. *Phys. Chem. Miner.* 35, 189–195.
- Sugahara, M., Yoshiasa, A., Yoneda, A., Hashimoto, T., Sakai, S., Okube, M., Nakatsuka, A., Ohtaka, O., 2008. Single-crystal X-ray diffraction study of  $\text{CaIrO}_3$ . *Am. Mineral.* 93, 1148–1152.
- Thompson, P., Wood, I.G., 1983. X-ray Rietveld refinement using Debye–Scherrer geometry. *J. Appl. Cryst.* 16, 458–472.
- Toby, B.H., 2001. EXPGUI, a graphical user interface for GSAS. *J. Appl. Cryst.* 34, 210–221.